A STUDY ON NUMERICAL DETERMINATION OF PERMEABILITY AND INERTIA COEFFICIENT OF ALUMINUM FOAM USING X-RAY MICROTOMOGRAPHY TECHNIQUE: FOCUS ON INSPECTION METHODS FOR RELIABILITY (PERMEABILITY AND INERTIA COEFFICIENT BY TOMOGRAPHY)

Hasan Celik,[1,2] Moghtada Mobedi,[3,] Akira Nakayama,[2,4] &*
Unver Ozkol[1]

[1]*Izmir Institute of Technology, Mechanical Engineering Department, 35430 Urla Izmir, Turkey*

[2]*Shizuoka University, Department of Mechanical Engineering, 3-5-1 Joho-ku, Naka-ku, Hamamatsu 432-8561, Japan*

[3]*Shizuoka University, Faculty of Engineering, 3-5-1 Joho-ku, Naka-ku, Hamamatsu 432-8561, Japan*

[4]*Wuhan Polytechnic University, School of Civil Engineering and Architecture, Wuhan, Hubei 430023, China*

*Address all correspondence to: Moghtada Mobedi, Shizuoka University, Faculty of Engineering, 3-5-1 Joho-ku, Naka-ku, Hamamatsu 432-8561, Japan; Tel./Fax: +81-53-478-8561, E-mail: moghtada.mobedi@shizuoka.ac.jp

The volume-averaged (i.e., macroscopic) transport properties such as permeability and inertia coefficient of two aluminum foams with 10 and 20 pores per inch (PPI) pore density are found using microtomography images. It is shown that a comparison between the numerical values and the experimental results may not be sufficient to prove the correctness of the obtained results. Hence, in addition to traditional validation methods such as grid independency and comparison with reported results in literature, further inspections such as (a) checking the development of flow, (b) inspection of Darcy and non-Darcy regions, (c) conservation of flow rate through the porous media, (d) sufficiency of number of voxels in the narrow throats, and (e) observation of transverse velocity gradients in pores for high and low Reynolds numbers can be performed to further validate the achieved results. These techniques have been discussed and explained in detail for the performed study. Moreover, the obtained permeability and inertia coefficient values are compared with 19 reported theoretical, numerical, and experimental studies. The maximum deviation between the present results and the reported studies for 10 PPI is below 25%, while for 20 PPI it is below 28%.

KEY WORDS: *pore scale analysis, permeability, microtomography, porous media*

1. INTRODUCTION

A literature survey shows that two main approaches are employed for heat and fluid flow simulations in porous media such as metal foams. One of these approaches is known as the pore scale method (PSM). In this method, the

NOMENCLATURE

$\langle\rangle$	volume-averaged quantity		V	volume [m^3]
$\langle\rangle^x$	intrinsic volume-averaged quantity			
			Greek Symbols	
A	coefficient defined in Eq. (9)		ε	porosity
B	coefficient defined in Eq. (9)		ρ	density [kg/m^3]
C	inertia coefficient		μ	dynamic viscosity [Pa s]
d	diameter [m]		ν	kinematic viscosity [m^2/s]
p	pressure [Pa]		Π	dimensionless pressure gradient
Re	Reynolds number			
K	permeability [m^2]		**Subscripts/Superscripts**	
u	velocity component [m/s]		c	cell
$\vec{V}$	velocity vector [m/s]		f	fluid

governing equations for the considered problem are solved in pore scale. Even though this method yields accurate results for velocity, temperature, and pressure fields, its application is very cumbersome and impractical due to the huge number of pores. To overcome this difficulty, the volume-averaged method (VAM) is suggested. VAM is easier compared to PSM since the governing equations are integrated over a representative volume of porous media, and volume-averaged governing equations (i.e., macroscopic governing equations) are obtained and the discontinuity of the phases is removed. Hence, the achieved governing equations can be solved for the entire space (Ucar et al., 2013). The main difficulty of VAM is new terms, involving volume-averaged transport parameters (i.e., macroscopic transport parameters), appearing in the volume-averaged equations. The volume-averaged transport parameters need to be known in order to apply VAM. VAM yields almost-accurate results as long as the values of the volume-averaged transport parameters are reliable (Vafai, 2015).

Volume-averaged transport properties can be obtained experimentally and/or theoretically. Recent developments in computing technology and microimaging techniques allow researchers to predict accurate volume-averaged transport parameters numerically using microtomography. One of the reported studies on determining the permeability and inertia coefficient of metal foams using microtomography was done by Petrasch et al. (2008). They studied the determination of permeability and inertia coefficient of reticulate porous ceramics using microtomography. The pore scale Re number was changed from 2 to 200 in their study. Magnico (2009) analyzed the determination of permeability tensors by computational fluid dynamics (CFD) from creeping flow to inertial flow for isotropic and anisotropic metallic foams. It was concluded that the Darcy–Forchheimer law is valid for Re > 1 and the inertial coefficient tensor can be asymmetric. Akolkar and Petrasch (2012) studied two kinds of porous media, reticulated porous ceramic foam and a packed bed of CaCO$_3$ particles, using pore scale analysis. The permeability and the Dupuit–Forchheimer coefficients were determined and different models for predicting permeability are compared. Microtomography-based CFD simulation of flow and heat transfer for three different open-cell aluminum foam samples with different pore densities varying between 10 and 30 pores per inch (PPI) were studied by Ranut et al. (2014, 2015). They concluded that flow and thermal simulations have an isotropic behavior for 30 PPI foam. On the contrary, a directional dependence on the computed flow permeability and effective thermal conductivity has been evinced for the 20 and 10 PPI foams. CFD characterization of flow regimes inside the open-cell aluminum foams was done by Della Torre et al. (2014). They studied the transition of flow from the laminar to the turbulent regime in an idealized foam by means of unsteady numerical simulations. They used a 40 PPI aluminum metal foam and modified the pore density into 10, 20, and 80 PPI from the original 40 PPI sample using dilation of the geometry. Microtomography-based numerical simulation of fluid flow and heat transfer in open-cell metal foams was done by Zafari et al. (2014, 2015). They considered local nonequilibrium thermal conditions between solid and fluid in their simulations. They showed that by changing the solid material from aluminum to copper, a significant increase in the effective stagnant thermal conductivity

takes place. Numerical investigation of pressure drop and heat transfer through metal foams and comparison against experiments were completed by Diani et al. (2015). Copper foams with 5, 10, 20, and 40 PPI were considered in their study. They showed a good agreement of the results of microtomography with experimental and theoretical results. The effect of strut shape of open-cell metal foams on the interfacial convection heat transfer and pressure drop was studied by Ambrosio et al. (2016). Three aluminum metal foam samples with porosities of 0.88, 0.94, and 0.97 were considered in their study. They concluded that the convex strut shape maximizes the convection heat transfer and minimizes the pressure drop for every porosity and velocity considered in their study.

The above literature survey presents part of the reported simulation studies on pore scale analysis of heat and fluid flow in porous media. Further simulation studies using microtomography images for applications from rocks to bones can be found in literature. These studies show that the use of micro- or even nanotomography for determination of transport parameters will become more popular in the future. However, similar to other computational studies, a high risk of numerical mistakes exits in the computational process. Hence, some techniques for testing of results at each step of the process are required.

In this study, two open-cell aluminum foams are scanned using an X-ray microtomography device. The obtained images are processed and a 3D representation of the real porous structure is created in a computer environment. Following this step, mesh is generated for the structure and the governing equations are solved numerically for the constructed mesh. The velocity and pressure distributions in the pores are obtained by solving continuity and momentum equations. Finally, the volume-averaged properties are found from the distributions of velocity and pressure. As mentioned before, this method is applicable for many porous materials as long as they can be scanned tomographically, such as rock, biomedical materials, packed beds, sandstone, or industrial porous products (Ucar et al., 2015; Liu and Wu, 2016; Notarberardino et al., 2008; Piller et al., 2013; Zhelezny et al., 2006).

The aim of this study is to develop and suggest techniques for inspection of CFD results for permeability and inertia coefficients at each step of the microtomography technique. Traditional validation methods (grid independency and comparison with an experimental result) do not show the reliability of obtained results and the agreement between the numerical and experimental results might be by chance. Further inspection methods for each step of the procedure are required to evaluate the obtained CFD results. The present work develops and suggests the required inspection methods. The suggested techniques can be applied for any employed software and codes. The authors recommend that the suggested inspection and validation methods be shown in the reports and papers to indicate that the predicted results are reliable. This paper is useful for researchers in this field to ensure the accuracy of achieved numerical results.

2. THE ANALYZED SAMPLES AND RECONSTRUCTED DOMAIN

X-ray computed microtomography is one of the widely used nondestructive methods for analyzing the structure of materials. In a micro-CT scanner, an X-ray beam cone passes through the sample and is collected by a detector. The sample is rotated, providing a series of 2D projection images at different angles. After completing the scanning process, the digital structure of the sample may be obtained in a computer environment from 2D images. In this study, the aluminum foam samples with a pore density of 10 and 20 PPI and with dimensions of $40 \times 40 \times 35$ mm^3 for 20 PPI and $40 \times 40 \times 20$ mm^3 for 10 PPI were received from the manufacturer as shown in Fig. 1(a). Since the determination of velocity and pressure for the entire sample is expensive due to the limitations on computational resources, tomography images were obtained only for a representative elementary volume (REV) with a size of $12 \times 12 \times 12$ mm^3 as shown in Fig. 1(b), which is satisfactory for our purposes. The studied REV is scanned using 9×9 μm^2 as the pixel size and 13.6 μm as the voxel length. This means that the number of pixels in both the x and y directions is 1400 and the number of images is 927. Following that, the obtained images are processed by ImageJ software and 3D domain is obtained as a stereolithography (STL) file. Structural properties of the analyzed foams, such as surface area and ligament thickness, are given in Table 1.

After obtaining an STL file, the snappyHexMesh mesh generator of the OpenFOAM CFD package is used to generate hexahedral mesh for the obtained 3D domain. The generated mesh for aluminum foam with 10 and 20 PPI is shown in Fig. 2. For numerical calculations, the supercomputer systems of Kyoto University in Japan and TUBITAK (Scientific and Technological Research Council of Turkey) in Turkey and different available workstations
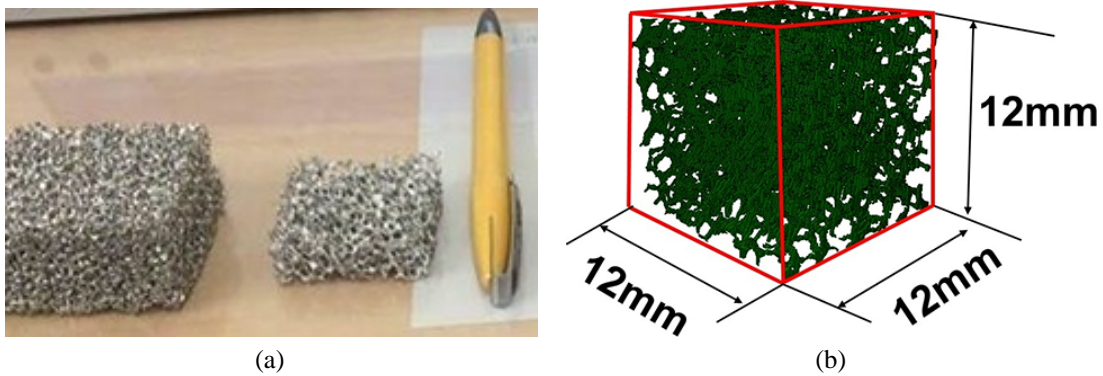
FIG. 1: Studied 10 PPI and 20 PPI pore density metal foams: (a) real structure and (b) domain generated in a computer environment (20 PPI)

TABLE 1: Properties obtained from the digital 3D model and the obtained results

Sample No.	1	2
Pore Density	10 PPI	20 PPI
Material	Al T-6201	Al T-6201
Porosity	0.90	0.95
Cell Diameter	0.0044	0.0023
Strut Diameter	0.00028	0.00019
Surface Area	0.0015	0.00277
K_{xx}	1.60×10^{-7}	8.97×10^{-8}
K_{yy}	2.33×10^{-7}	9.66×10^{-8}
K_{zz}	2.56×10^{-7}	1.11×10^{-7}
K **Average**	1.83×10^{-7}	9.92×10^{-7}
C_{xx}	0.2054	0.1125
C_{yy}	0.1303	0.0925
C_{zz}	0.0975	0.1253
C **Average**	0.1359	0.1101

with different types of central processing units are used. For instance, the CPU time was around 8 h for the computer at TUBITAK, a Xeon E5-2690 with 72 CPU, in parallel for Re = 600 and PPI = 20.

3. PORE SCALE FLOW ANALYSIS AND COMPUTATIONAL DOMAIN

Following the mesh generation, flow in the pore scale can be analyzed computationally. Air is considered as a Newtonian working fluid and flow is steady state. The effect of gravity is neglected. Under these assumptions, the following governing equations of conservation of mass and momentum are solved to find velocity and pressure in the voids:

$$\nabla \cdot \overrightarrow{V} = 0 \tag{1}$$

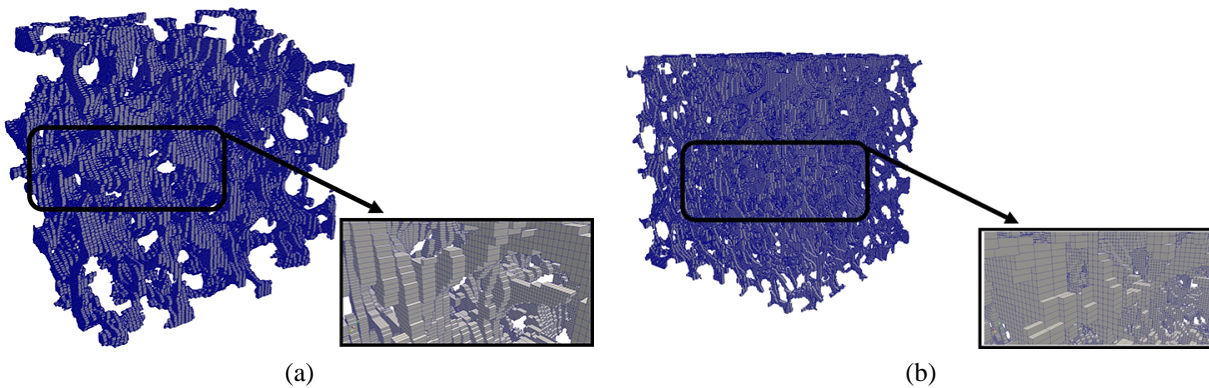(a)   (b)

FIG. 2: Domain generated in a computer environment: (a) 10 PPI metal foam and (b) 20 PPI metal foam

$$\left(\vec{V} \cdot \nabla\right) \vec{V} = \frac{1}{\rho} \nabla p + \nu \nabla^2 \vec{V} \tag{2}$$

where $\vec{V}$ is the velocity vector, p is the pressure, and $\rho\nu$ are the density and kinematic viscosity of air. The values of ρ and ν are taken into account at the reference temperature of 293.15 K.

Dummy regions are added to the computational domain behind and after the metal foam section in order to reduce the inlet and outlet effects as shown in Fig. 3. The dimensions of this region are taken to be the same as the length of the metal foam region. OpenFOAM 2.3.1 is used to solve the continuity and momentum equations for the flow in the voids of metal foams. The code has been written based on the finite volume approach. The coupling of velocity and pressure is treated by the SIMPLE algorithm. The convergence criterion is set to 10^{-6} for all the terms in the governing equations.

A uniform velocity is applied for the inlet section and the boundary condition of zero gradient for velocity is applied for the outlet referring to the negligible diffusion transport. A slip boundary condition is applied for the lateral walls of the channel in order to reduce the effect of the walls on the flow field. The computational domain and boundary conditions are also shown in Fig. 3. Although in Fig. 3 the computational domain is shown for flow in the y direction, similar domains can be employed for x and z directions to find out the degree of isotropic feature of metal
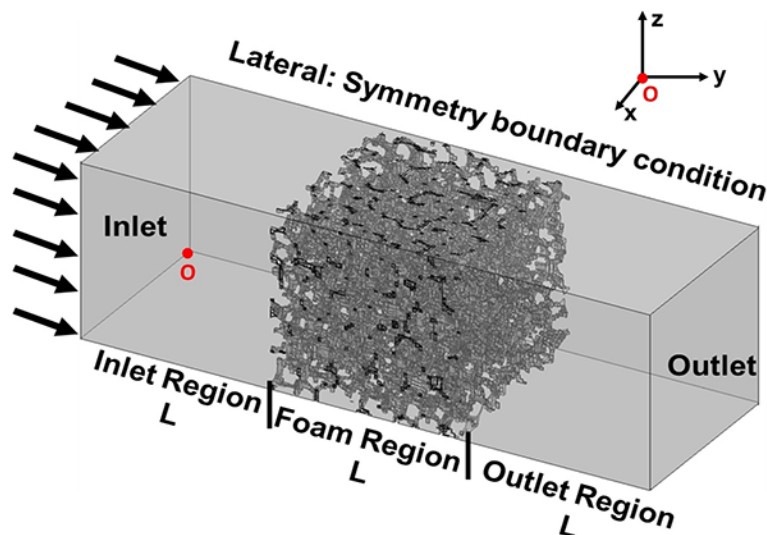

FIG. 3: Considered domain with dummy inlet and outlet regions, and boundary conditions (O indicates the origin point)

foam. This means that the velocity and pressure fields in the same voids but for different principal flow directions are obtained separately.

4. DETERMINATION OF PERMEABILITY AND INERTIA COEFFICIENTS

In VAM, the volume-averaged conservation of mass and momentum equations are used to find the volume-averaged velocity and pressure. For an REV quantity with a volume of V, two types of volume averaging exist:

$$\langle \varphi \rangle = \frac{1}{V} \int_V \varphi dV \tag{3}$$

$$\langle \varphi \rangle^x = \frac{1}{V_x} \int_{V_x} \varphi dV \tag{4}$$

which are called volume average and intrinsic volume average of φ quantity, respectively. In this study φ can be velocity or pressure. Using these definitions, for steady and laminar flow, the continuity and momentum equations can be written as

$$\nabla \cdot \left\langle \overrightarrow{V} \right\rangle = 0 \tag{5}$$

$$\frac{1}{\varepsilon^2} \left\langle \overrightarrow{V} \right\rangle \cdot \nabla \left\langle \overrightarrow{V} \right\rangle = -\frac{1}{\rho_f} \nabla \langle p \rangle^f + \frac{\mu}{\varepsilon} \nabla^2 \left\langle \overrightarrow{V} \right\rangle - \frac{\mu}{\rho_f K} \left\langle \overrightarrow{V} \right\rangle - \frac{C}{\sqrt{K}} \left| \left\langle \overrightarrow{V} \right\rangle \right| \left\langle \overrightarrow{V} \right\rangle \tag{6}$$

where K is the permeability tensor and C is the inertia coefficient. In many porous media applications, the effects of the term on the left side (convection term) and the second term on the right side (which represents the effects of volume-averaged pure viscous forces) are small compared to the other terms of Eq. (6). If a unidirectional flow is considered, Eq. (6) takes the following form, which is usually called the Darcy-extended Forchheimer equation:

$$\nabla \langle p \rangle^f = -\frac{\mu}{K} \langle u \rangle - \frac{C}{\sqrt{K}} \rho_f \langle u \rangle^2 \tag{7}$$

Equation (7) can be expressed in dimensionless form as follows:

$$\Pi = A + B\mathrm{Re} \tag{8}$$

The dimensionless parameters of A, B, and Π are defined as

$$\Pi = -\frac{d_c^2}{\langle u \rangle \mu_f} \frac{d \langle p \rangle^f}{dx}, \quad A = \frac{d_c^2}{K}, \quad B = C \left(\frac{d_c^2}{K} \right)^{1/2}, \quad \mathrm{Re} = \frac{\rho_f \langle u \rangle d_c}{\mu_f} \tag{9}$$

where d_c is the cell diameter selected as the characteristic length. Both cell and pore diameters can be selected as the characteristic length, and in this study cell diameter is chosen. For determination of average pore and cell diameters, the diameter of some random cells in the metal foam in a computer environment is measured. The average of the measured values is accepted as the pore or cell size. The average cell diameters were found to be 2.3 mm for 20 PPI and 4.4 mm for 10 PPI. A sample of the cell for which the pore diameter is measured is shown in Fig. 4. To determine the values of K and C, two methods are used in the literature: the linear (or dimensionless linear) and parabolic approaches. The dimensionless linear approach enabling the prediction of the critical Reynolds number for separation of Darcy from non-Darcy regions is used in this study (Ucar et al., 2015). In this method, first the volume-averaged velocity and pressure drop at cross sections perpendicular to the flow direction is calculated. Then the change of pressure drop in the flow direction is drawn to obtain the pressure gradient in the flow direction by employing a proper curve-fitting method, and the dimensionless pressure drop for the specified Re number can be obtained from Eq. (9). The same method can be employed to determine the dimensionless pressure drop for different Re numbers. Then the dimensionless pressure can be plotted against the Re number, and finally, by applying a proper curve-fitting method, Eq. (7) and the coefficients of A and B can be found. The permeability and inertia coefficients can be obtained from A and B values.
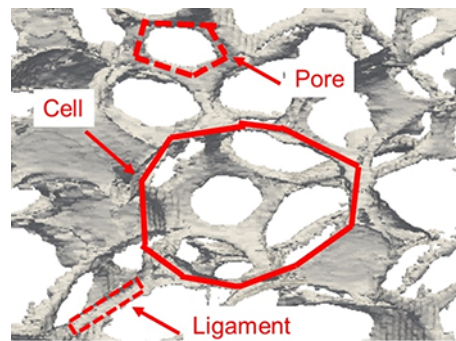
FIG. 4: Sample of obtained views for determination of structural properties generated in computer environment by microtomography images

5. SUGGESTED INSPECTION TECHNIQUES FOR VALIDATION

The flow field in the digital structure of the generated porous media can be obtained by solving continuity and momentum equations for flow in the voids. Finding the permeability and inertia coefficient from the velocity and pressure field was described before. Although it seems simple, due to irregular pores and voids, the risk of obtaining wrong results is high. Hence, some checks are required to be sure of the solution. In this section, the possible checks and inspections for the computational procedure and obtained results are described.

5.1 Verification for Elimination of Images

Digital image processing is a challenging task. A high amount of RAM and CPU resources are required to obtain high-quality 3D views. The number of image slices taken through the domain affects the voxel length (i.e., the distance between two slices). No doubt the decrease in distance between the images increases the accuracy of the results; however, the high number of images considerably affects the computational resources required to process the images. Therefore, some images can be eliminated for the sake of computational resources. In this study, due to the limitation of computational resources, the effect of image number on the results is studied and an obtained result for Re = 600 is given in Fig. 5(a). As can be seen, for a low number of images (15) the permeability in the flow direction changes by increasing the number of images; however, after a reasonable number of images, further increasing the number does not influence the results. It is seen that 309 images per 12.32 mm (i.e., 40 μm as voxel length) might be sufficient to obtain acceptable permeability and inertia coefficient values for the problem considered in this study. For each image the number of pixels is 1400×1400.

5.2 Verification of Grid Numbers

The permeability and inertia coefficient values are calculated for grid numbers from $24 \times 24 \times 24$ to $250 \times 250 \times 250$, and the changes for Re = 600 are shown in Figs. 5(b) and 5(c), respectively. A cell number around 7,000,000 is sufficient to have accurate results. Furthermore, Fig. 6 shows the change of digital porous structure with the number of grids in the transverse direction. By changing the grids from $48 \times 48 \times 48$ to $148 \times 148 \times 148$, the generated structure considerably changes. Not only the size but also the location of the solid phase and voids change. However, by changing the grids from $148 \times 148 \times 148$ to $192 \times 192 \times 192$ or $250 \times 250 \times 250$, the size and location of the ligaments do not vary, indicating independency of the generated structure from the mesh.

5.3 Check of the Flow Rate and Velocity through Metal Foam

Whether or not the volumetric flow rate through metal foam remains constant must be checked as a first step to see if the conservation of mass is satisfied by the numerical scheme. Both the intrinsic flow rate in some cross sections and
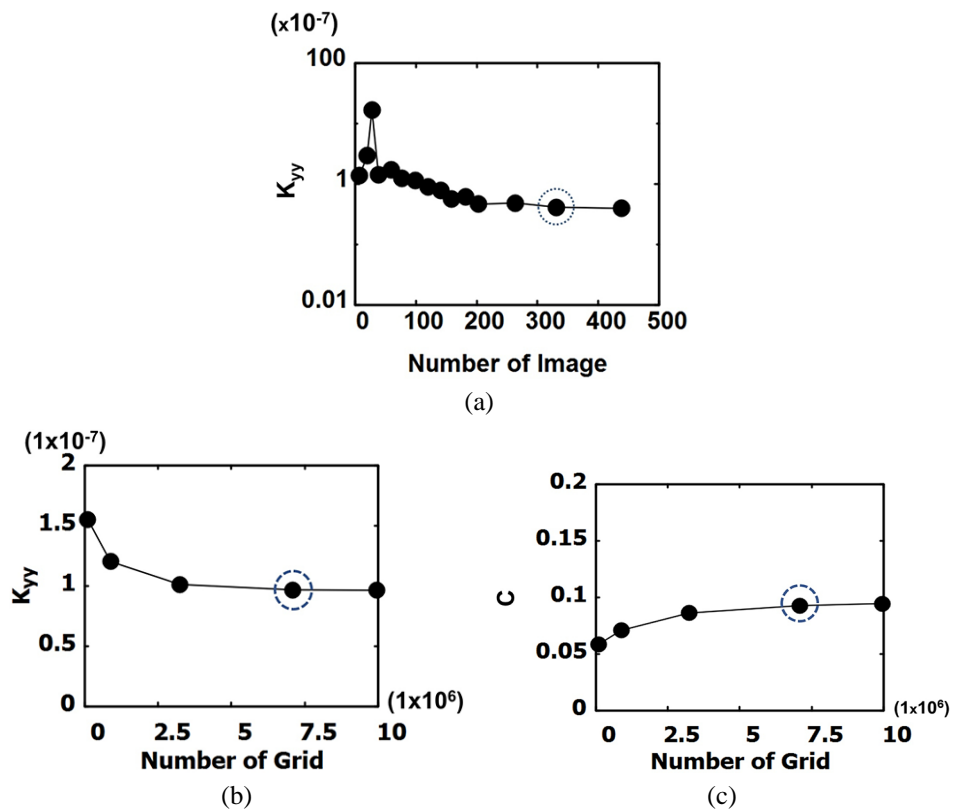
FIG. 5: Validation of number of images and grids for Re = 600: (a) the change of permeability in the y direction with respect to number of images in the flow direction, (b) the change of permeability in the y direction with respect to grid number, and (c) the change of inertia coefficient in the y direction with respect to grid number
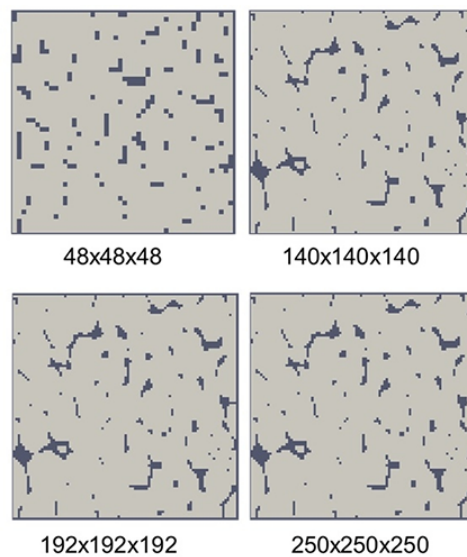

FIG. 6: Change of the generated structure of aluminum foam (PPI = 20) with number of grids for the surface with $y = 3L/2$ (black is solid region while gray represents voids)

the area of those cross sections can be calculated and plotted. For unidirectional flow in an isotropic porous media, the intrinsic flow rate should be identical through the directional flow. Furthermore, the intrinsic averaged velocity for each cross section should have a reverse trend with the area of the cross section. The aforementioned check was done in this study for metal foam with 10 and 20 PPI and Reynolds number of 0.001 and 600. As can be seen from Fig. 7, the volumetric flow rate remains constant for two metal foams at both Reynolds numbers, and by decreasing or increasing the passage area, the air velocity appropriately increases or decreases.

5.4 Check of Existence of Fully Developed Region

The application of Eq. (7) for a constant volume-averaged velocity is possible when a constant pressure drop exists in the flow direction—in other words, when a fully develop flow exists. Figure 8 shows two samples of the change of pressure drop through the computational domain for Re = 0.001 and 600. The pressure change in the dummy regions is negligible, while a steep linear gradient is seen for the porous region. These charts not only prove the existence of fully developed flow in the porous media region but also yield an accurate value of the pressure gradient through the porous media by using an accurate curve-fitting program.
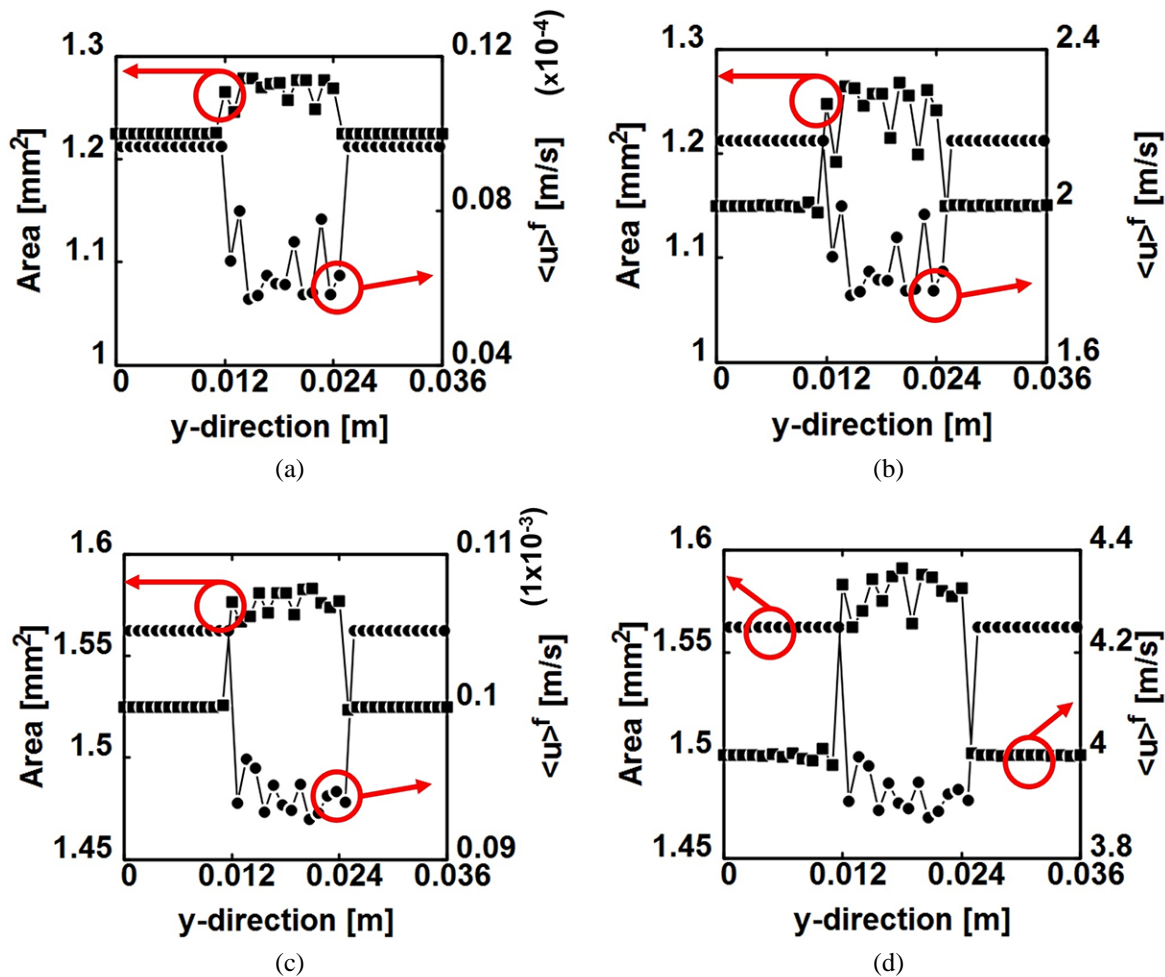

FIG. 7: Change of volume-averaged velocity and cross-sectional area through the domain: (a) Re = 0.001 and 10 PPI, (b) Re = 600 and 10 PPI, (c) Re = 0.001 and 20 PPI, and (d) Re = 600 and 20 PPI
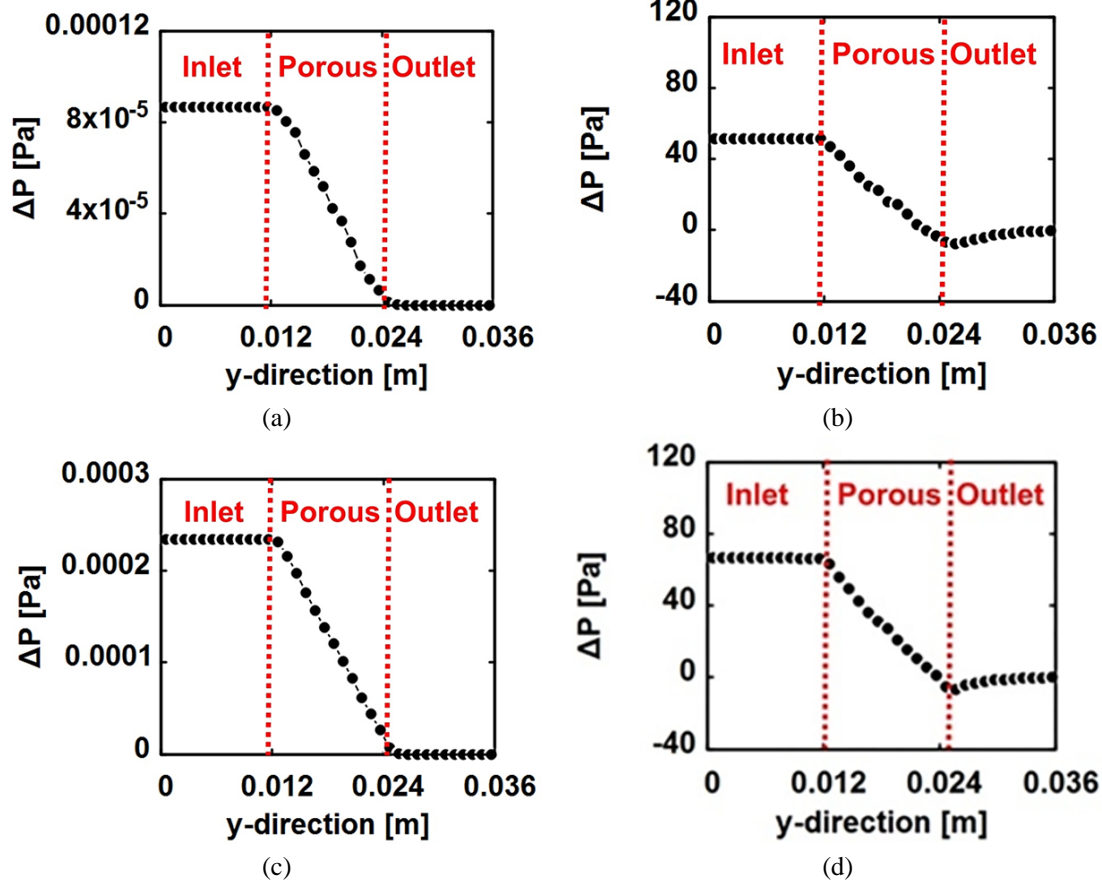
FIG. 8: Change of pressure gradient through the domain when (a) Re = 0.001 and 10 PPI, (b) Re = 600 and 10 PPI, (c) Re = 0.001 and 20 PPI, and (d) Re = 600 and 20

5.5 Check of Darcy and Non-Darcy Region

There is no doubt that the permeability value can be calculated by determination of the pressure gradient through the porous media and using the Darcy equation. Similarly, by determination of three pressure values through the porous media and using the Darcy-extended Forchheimer equation, both the permeability and inertia coefficients can also be calculated. However, these methods not only do not yield accurate results but also do not specify whether flow is in the Darcy or non-Darcy region. The advice of the authors is to a obtain sufficient number of pressure gradients for different velocities and then measure the change of dimensionless pressure drop with Reynolds number, as seen in Fig. 9. The drawing of this diagram allows us (a) to find out the critical Reynolds number to separate the Darcy from the non-Darcy region, (b) to verify the obtained results for low values of Re number and small changes of Π (however, a linear change of Π exists for high values of Re), (c) to prevent the use of a wrong equation (for instance, the use of the Darcy equation when the flow may involve the inertia effect), and finally (d) to remove small numerical mistakes by applying appropriate curve fitting to the large number of numerically obtained points.

5.6 Number of Voxels in Narrow Throats

Based on the structure, the number of voxels in a narrow throat (narrow pores) may be an important parameter showing the accuracy of the results. The shrinking and expansion of the pores plays an important role in the pressure drop in porous media. Hence, a sufficient number of voxels should exist in the throats to simulate flow in the pore
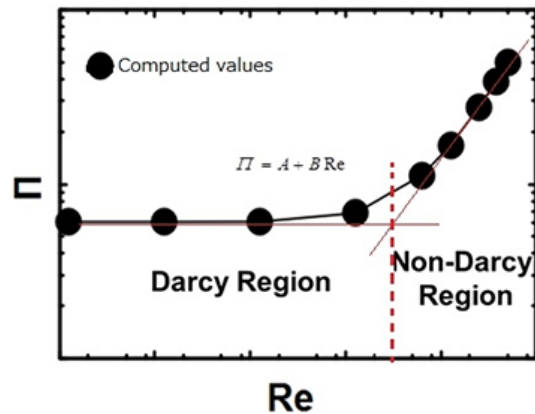
FIG. 9: Schematic view for the determination method for Darcy and non-Darcy regions (thin line shows extreme cases and vertical dash line separates the regions)

scale accurately. Figure 10 shows a cross section of voxels perpendicular to the flow. It can be easily seen that the number of voxels in the cells and throats (pores) is sufficient for accurate determination of flow and pressure drop.

5.7 Check of Velocity Gradient in Transverse Direction for Low and High Reynolds Number

Similar to the flow in the channel and pipe, there should be a velocity gradient near the solid surface, and with an increase of Re number, the velocity gradient near the surface region must increase. Hence, there should be a sufficient number of voxels in the pores to deduce this fact. Figure 11 shows the velocity profile in the middle line of a cross section. Figure 11(a) shows velocity profiles for Re = 0.001. As can be seen, a smooth flow exists in the pore, and a velocity gradient on the region close to the surface can be observed. By increasing the Re number from 0.001 to 600, the gradient near the surface increases, and furthermore, fluctuations due to colliding of the flow to the front ligament appear [see Fig. 11(b)]. This figure provides a level of confidence in the employed number of voxels in the pores.

5.8 Comparison with Reported Studies

Even though the porosity and macroscopic structure of the two porous media are the same, the pore scale geometrical differences change the values of the macroscopic transport parameters. Hence, in order to compare the transport
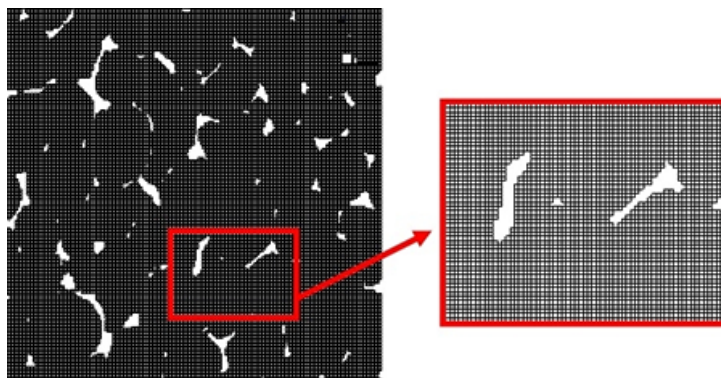

FIG. 10: Generated mesh in the middle cross section of the foam region ($y = 3L/2$) perpendicular to the flow (20 PPI)
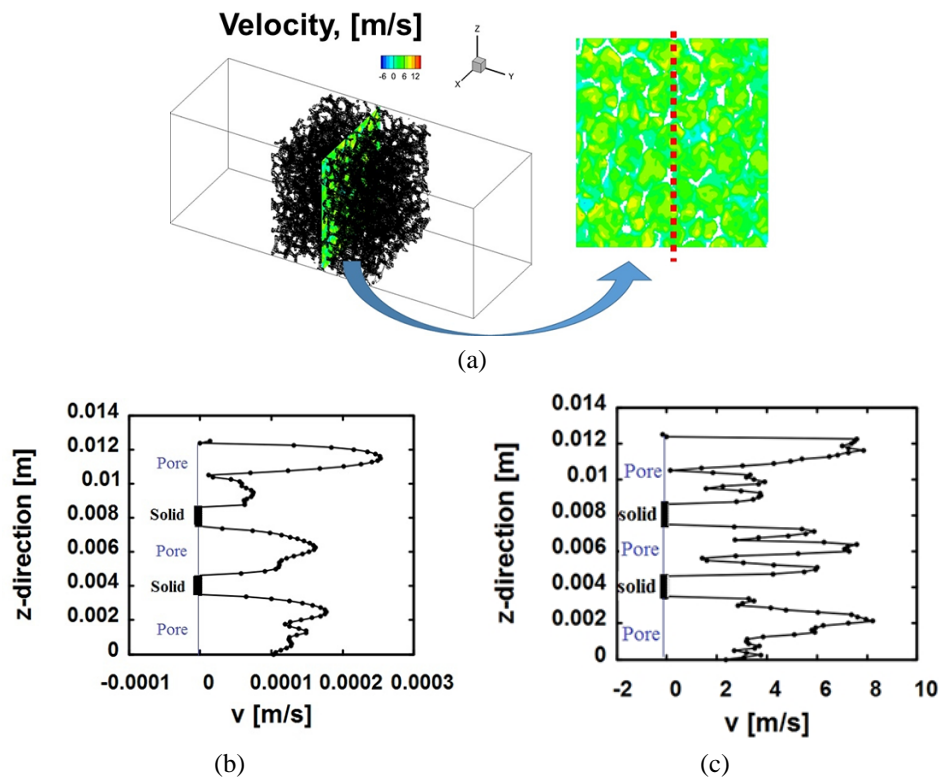
FIG. 11: Velocity profiles on the line at the midpoint for 20 PPI metal foam: (a) the considered line to plot the velocity profile, (b) the velocity profile at the midplane [vertical dash line in Fig. 11(a)] when Re = 0.001, and (c) the velocity profile at the midplane [vertical dash line in Fig. 11(a)] when Re = 600

parameters of two porous media, detailed information about the structural descriptors must be known. Unfortunately, some researchers describe the studied porous media (such as metal foam) by using only the porosity and PPI, which are not sufficient to specify a porous structure for comparison. Hence, finding the proper experimental or numerical results from literature for comparison is not an easy task. Table 1 shows the value of the other governing parameters such as pore diameter, cell diameter, strut thickness, and specific surface area of the two aluminum foams considered in this study.

6. RESULTS

After presenting inspection methods for checking the employed software and the applied calculation process, the obtained results are described in this section. Figure 12 shows the change of velocity contour in the flow direction at the midsection slice through the flow direction of the metal foam with 20 PPI. It is plotted for four Re number as 0.001, 12, 26, and 600. The white regions show the solid parts in porous medium. The contour range (i.e., legend) is identical for four Re numbers. The Darcy velocity is 1 mm/s for Re = 0.001, which is very low. Velocity distribution seems to be very uniform from this figure. By increasing the Re number, the velocity in the voids increases and distributions becomes more inhomogeneous, especially for Re = 600. The effect of tortuosity (complexity of the fluid path) can be seen clearly since in some pores the highest velocity is deviated from the middle of the voids. The same situation was also observed for aluminum foam with 10 PPI.

Figure 13 shows the change of velocity component in the flow direction through the channel of metal foam with 10 and 20 PPI and for Re = 600. As can be seen, a uniform velocity distribution exists in the inlet region since the cross-sectional area does not change. The velocity value increases in the voids of the metal foam due to reduction of
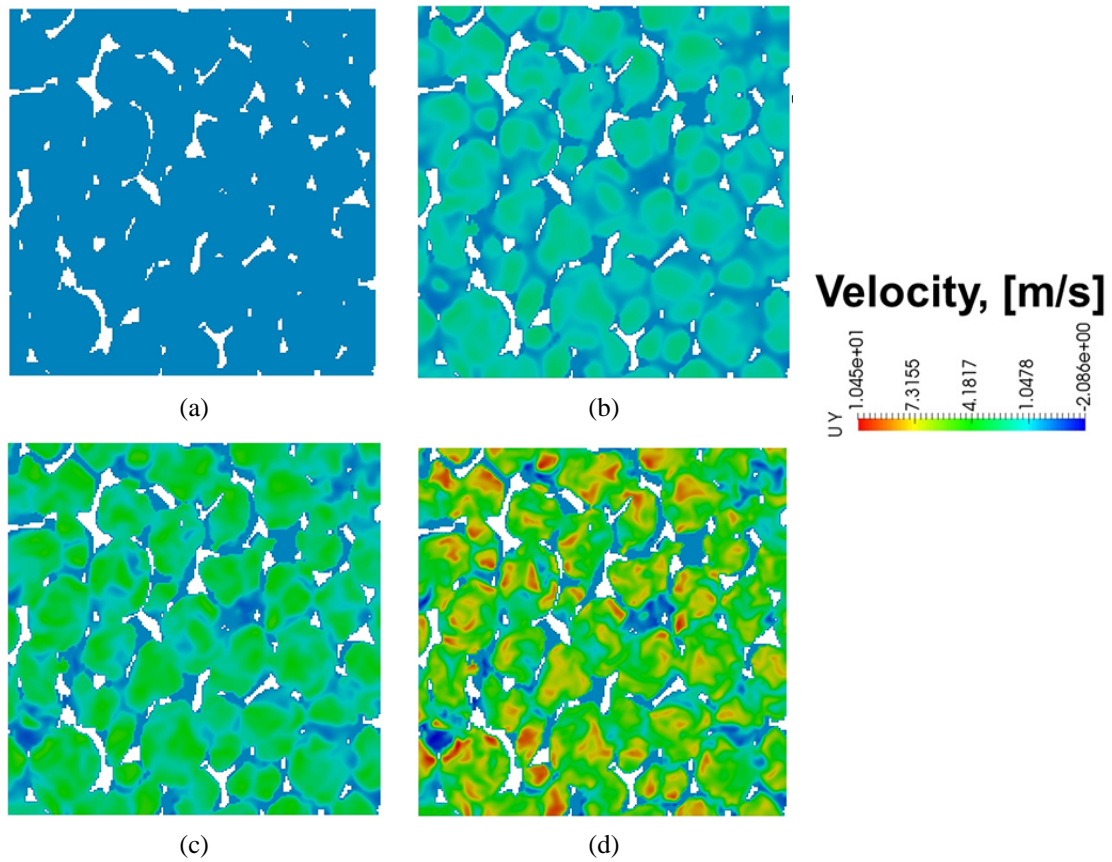
FIG. 12: Change of velocity contour in flow direction at the midsection slice of the metal foam with 20 PPI: (a) Re = 0.001, (b) Re = 12, (c) Re = 26, and (d) Re = 600
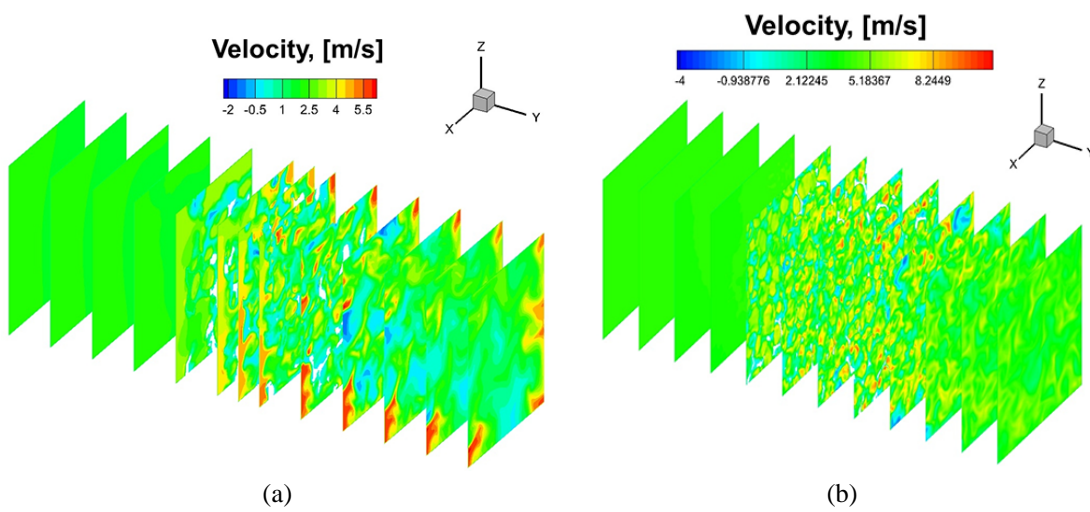

FIG. 13: Change of velocity component in flow direction through the channel of metal foam with Re = 600 for (a) 10 PPI and (b) 20 PPI

flow in the cross-sectional areas. Finally, there is almost no change in the outlet region. Because the slip boundary condition is applied to the circumference of the channel, nonuniformity near the boundaries is removed. Figure 14 shows the change of pressure in the same channel as Fig. 13. As expected, at the inlet of the channel the pressure is high, and through the channel it decreases. By changing the flow cross-sectional area in the porous media, a change of pressure gradient in the voids is seen. Finally, at the outlet of the channel, almost the lowest pressure gradient can be observed.

The present study is validated with the experimental and theoretical studies reported in the literature in terms of pressure gradient with change of velocity, for both 10 and 20 PPI foams. Deviations of $\pm$ 50% from the present results are also added into Fig. 15 and shown in red dashed lines. As can be seen, an acceptable agreement between the obtained and reported results can be observed. It will be impossible to achieve the same results of those studies since porosity, strut diameter, and surface area of the aluminum foams are different in each study. The manufacturers of those aluminum foams may also be different. For instance, from the porosity point of view, the porosity of the
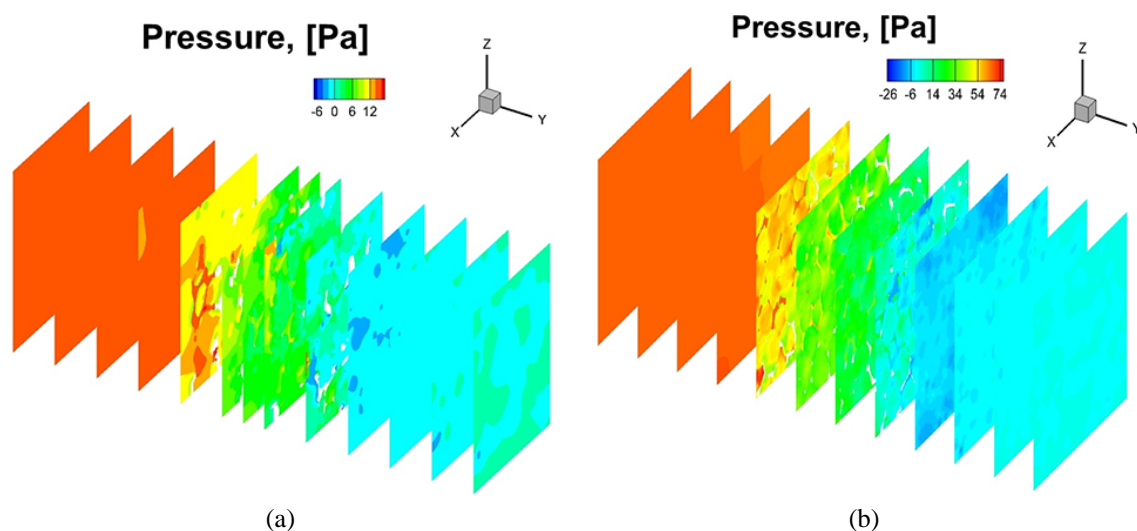

FIG. 14: Change of pressure through the channel of metal foam with Re = 600 for (a) 10 PPI and (b) 20 PPI
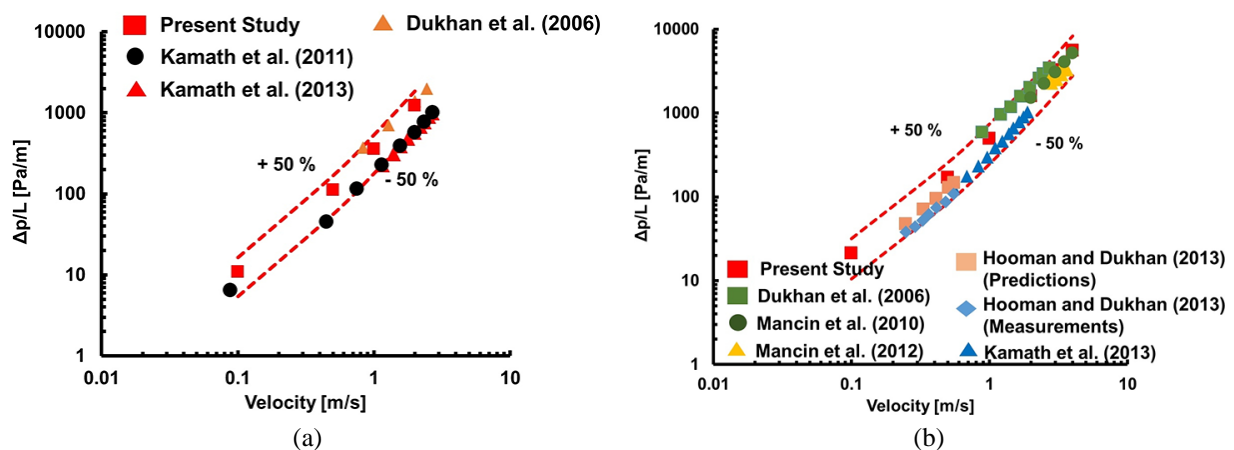

FIG. 15: Comparison of the pressure gradient with inlet velocity obtained in the present study with the reported experimental studies: (a) 10 PPI and (b) 20 PPI. [The compared studies: Kamath et al. (2011, 2013), Dukhan et al. (2006), Mancin et al. (2010, 2012), Hooman and Dukhan (2013)].

samples of Kamath et al. (2011, 2013), Mancin et al. (2010), and Hooman and Dukhan (2013) are 0.90, 0.90, 0.932, and 0.90, respectively, while for the present study the porosity of the studied 20 PPI sample is 0.948.

The changes of dimensionless pressure drop with Re numbers for aluminum foams with pore densities of 10 and 20 PPI and for x, y, and z principal axes are presented in Fig. 16. As seen here, the inertia effect is not significant until the Re number is around 1, since the value of Π remains constant. However, after Re $= 1$, the effect of inertia appears and Π changes linearly with Re in the non-Darcy region; consequently, the inertia effect should be taken into account. It should also be mentioned that the values of Π for x, y, and z directions are not the same and small changes between them exist. There could be two reasons for small differences. One is that there might be a small anisotropy in the sample, since the studied size is small. The second reason is the possibility that the elimination of images in the x direction causes a slight difference in the structure of the y direction from the x and z directions.

The obtained permeability and inertia coefficient for the principal axes of two aluminum metal foams is shown in Table 1. The change between the values of these transport properties is not too significant and the average of them can be accepted as the unique permeability and inertia coefficient. Figure 17 compares the obtained value with some of the reported results. It can be seen that many aluminum foams have different porosities and inertia coefficients but
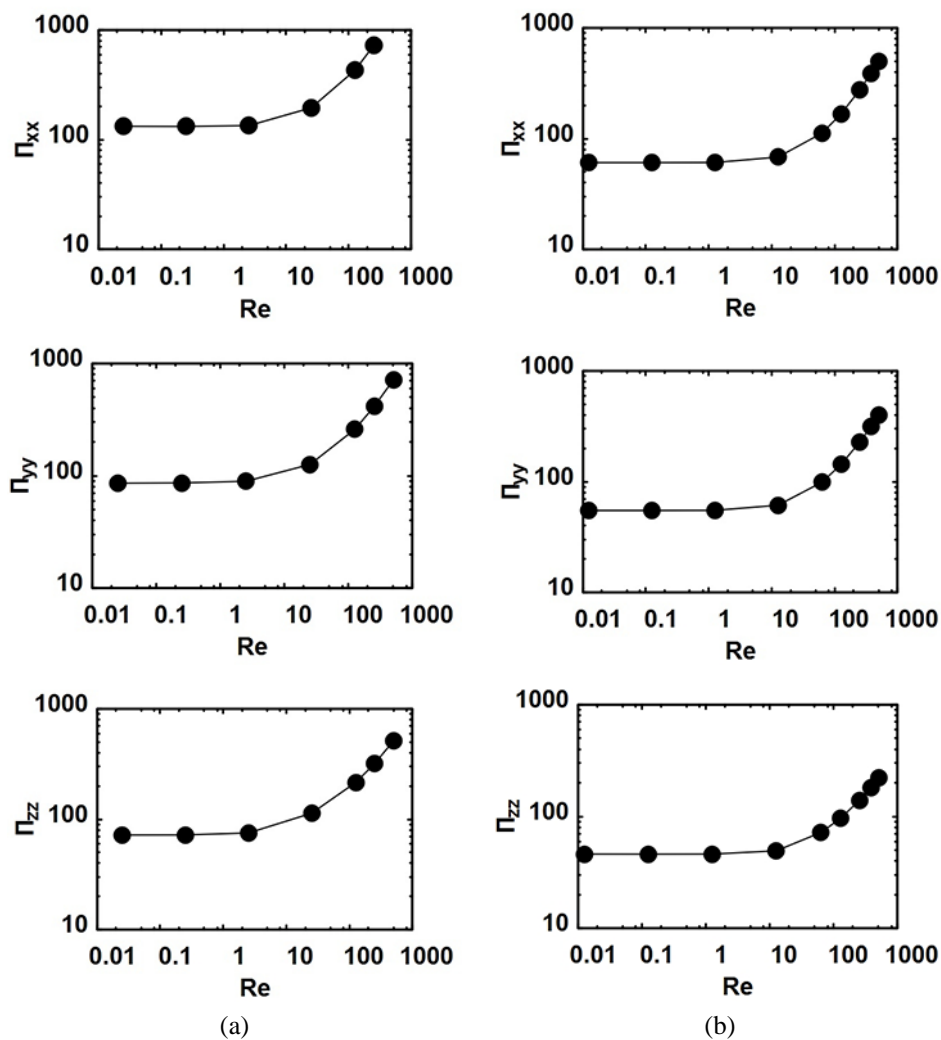

FIG. 16: Change of dimensionless pressure gradient with respect to Re number for (a) 10 PPI and (b) 20 PPI
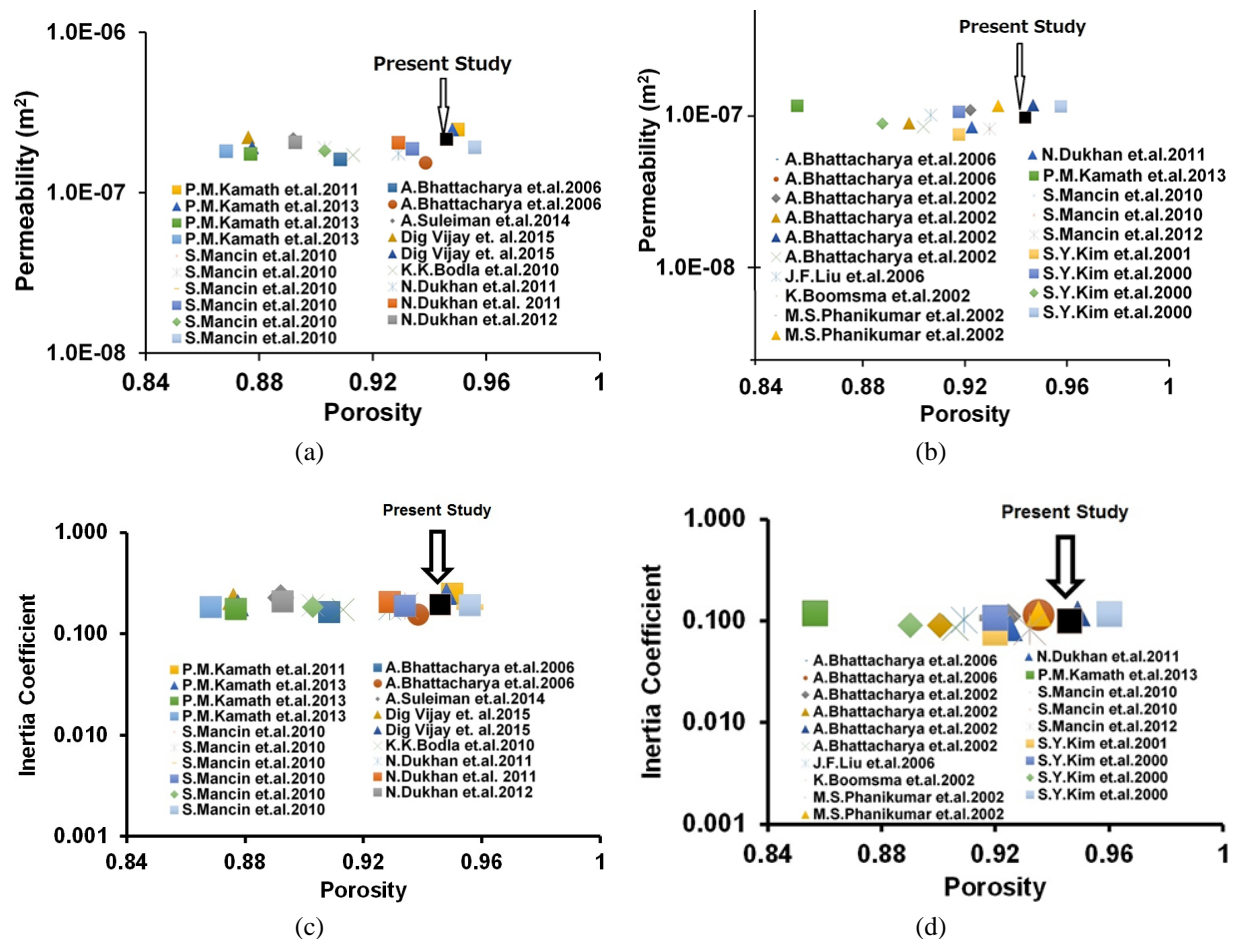
FIG. 17: Comparison of the present study with the reported studies in literature and the average of permeability of these reported studies in the literature: (a) permeability 10 PPI, (b) permeability 20 PPI, (c) inertia coefficient 10 PPI, and (d) inertial coefficient 20 PPI. [The compared studies: Kamath et al. (2011, 2013), Mancin (2010), Bhattacharya (2002), Bhattacharya and Mahajan (2006), Suleiman and Dukhan (2014), Vijay et al. (2015), Bodla et al. (2010), Dukhan and Patel (2011), Dukhan and Ali (2012), Liu and Wang (2016), Boomsma and Poulikakos (2002), Phanikumar and Mahajan (2002), Mancin et al. (2010, 2012), Kim et al. (2000, 2001)].

the same PPI. The obtained values for both permeability and inertia coefficient are in the range of the reported values. The difference between the obtained results and the results of the reported studies for 10 PPI is less than 25%, while for 20 PPI it is less than 28%.

7. CONCLUSION

The values of permeability and inertia coefficient for two aluminum metal foams were found computationally using microtomography images. After solving the continuity and momentum equations for the voids inside the metal foam, the volume-average technique is applied and the values of those transport parameters are found according to the Darcy-extended Forchheimer equation. A good agreement between the obtained values and reported experimental values was observed.

The main focus of the study is on techniques which can be employed to check the accuracy of the obtained results and to inspect the long computational process. In addition to the traditional checks such as grid independency,

comparison of results with available results in literature, and image reduction checks, significant inspections for the accuracy of the computational process are suggested and discussed. The suggested computational process inspection can be listed as follows:

- The number of voxels (or mesh) in the narrowest throat must be sufficiently high in order to simulate the flow properly.

- The fully developed flow condition must be checked to ensure that the application of the Darcy or Darcy-Forchheimer equation is valid.

- Calculations for both the Darcy and non-Darcy regions should be done in order to catch any computational mistake and find accurate coefficients from the dimensionless Darcy-Forchheimer equation.

- The mesh scale must be fine enough near the walls so that the transverse velocity gradient is resolved well in the pores.

- Conservation of mass must be checked. The simplest way to do this is to look at whether the flow rate stays the same at different cross sections through the flow direction.

There is no doubt that by improving computer and software technology, smaller voxels can be used, there is no need for elimination of images, and more accurate results can be achieved. Furthermore, computation can be done for larger samples to reduce the possible directional errors.

ACKNOWLEDGMENTS

REFERENCES

Akolkar, A. and Petrasch, J., Tomography-Based Characterization and Optimization of Fluid Flow through Porous Media, *Transp. Porous Media*, vol. **95**, pp. 535–550, 2012.

Ambrosio, G., Bianco, N., Chiu, W.K.S., Iasiello, M., Naso, V., and Oliviero, M., The Effect of Open-Cell Metal Foams Strut Shape on Convection Heat Transfer and Pressure Drop, *Appl. Therm. Eng.*, vol. **103**, pp. 333–343, 2016.

Bhattacharya, A., Calmidi, V.V., and Majahan, R.L., Thermophysical Properties of High Porosity Metal Foams, *Int. J. Heat Mass Transf.*, vol. **45**, pp. 1017–1031, 2002.

Bhattacharya, A. and Majahan, R.L., Metal Foam and Finned Metal Foam Heat Sinks for Electronics Cooling in Buoyancy-Induced Convection, *J. Electron. Packaging*, vol. **128**, pp. 259–266, 2006.

Bodla, K.K., Murthy, J.Y., and Garimella, S.V., Microtomography-Based Simulation of Transport through Open-Cell Metal Foams, *Numer. Heat Transf., Part A: Applications*, vol. **58**, no. 7, pp. 527–544, 2010.

Boomsma, K. and Poulikakos, D., The Effects of Compression and Pore Size Variations on the Liquid Flow Characteristics in Metal Foams, *J. Fluids Eng.*, vol. **124**, pp. 263–272, 2002.

Della Torre, A., Montenegro, G., Tabor, G.R., and Wears, M.L., CFD Characterization of Flow Regimes inside Open Cell Foam Substrates, *Int. J. Heat Fluid Flow*, vol. **50**, pp. 72–82, 2014.

Diani, A., Bodla, K.K., Rossetto, L., and Garimella, S.V., Numerical Investigation of Pressure Drop and Heat Transfer through Reconstructed Metal Foams and Comparison against Experiments, *Int. J. Heat Mass Transf.*, vol. **88**, pp. 508–515, 2015.

Dukhan, N. and Patel, K., Effect of Sample's Length on Flow Properties of Open-Cell Metal Foam and Pressure-Drop Correlations, *J. Porous Mater.*, vol. **18**, no. 6, pp. 655–665, 2011.

Dukhan, N. and Ali, M., Strong Wall and Transverse Size Effects on Pressure Drop of Flow through Open-Cell Metal Foam, *Int. J. Thermal Sci.*, vol. **57**, pp. 85–91, 2012.

Dukhan, N., Picón-Feliciano, R., and Álvarez-Hernández, A.R., Air Flow through Compressed and Uncompressed Aluminum Foam: Measurements and Correlations, *J. Fluid Eng.*, vol. **128**, pp. 1004–1012, 2006.

Hooman, K. and Dukhan, N., A Theoretical Model with Experimental Verification to Predict Hydrodynamics of Foams, *Transp. Porous Media*, vol. **100**, pp. 393–406, 2013.

Kamath, P.M., Balaji, C., and Venkateshan, S.P., Experimental Investigation of Flow Assisted Mixed Convection in High Porosity Foams in Vertical Channels, *Int. J. Heat Mass Transf.*, vol. **54**, no. 25, pp. 5231–5241, 2011.

Kamath, P.M., Balaji, C., and Venkateshan, S.P., Heat Transfer Studies in a Vertical Channel Filled with Porous Medium, *Fluid Dyn. Mater. Process*, vol. **9**, no. 2, pp. 109–124, 2013.

Kim, S.Y., Paek, J.W., and Kang, B.H., Flow and Heat Transfer Correlations for Porous Fin in a Plate-Fin Heat Exchanger, *J. Heat Transf.*, vol. **122**, no. 3, pp. 572–578, 2000.

Kim, S.Y., Kang, B.H., and Kim, J.H., Forced Convection from Aluminum Foam Materials in an Asymmetrically Heated Channel, *Int. J. Heat Mass Transf.*, vol. **44**, no. 7, pp. 1451–1454, 2001.

Liu, Z. and Wu, H., Pore-Scale Study on Flow and Heat Transfer in 3D Reconstructed Porous Media using Micro-Tomography Images, *Appl. Therm. Eng.*, vol. **100**, pp. 602–610, 2016.

Magnico, P., Analysis of Permeability and Effective Viscosity by CFD on Isotropic and Anisotropic Metallic Foams, *Chem. Eng. Sci.*, vol. **64**, pp. 3564–3575, 2009.

Mancin, S., Zilio, C., Cavallini, A., and Rossetto, L., Pressure Drop during Air Flow in Aluminum Foams, *Int. J. Heat Mass Transf.*, vol. **53**, no. 15, pp. 3121–3130, 2010.

Mancin, S., Zilio, C., Rossetto, L., and Cavallini, A., Foam Height Effects on Heat Transfer Performance of 20 PPI Aluminum Foams, *Appl. Therm. Eng.*, vol. **49**, pp. 55–60, 2012.

Notarberardino, B., Walker, B., and Abdul-Aziz, A., An Efficient Approach to Converting Three-Dimensional Image Data into Highly Accurate Computational Models, *Philos. Trans. Royal Soc. A*, vol. **366**, no. 1878, pp. 3155–3173, 2008.

Phanikumar, M.S. and Mahajan, R.L., Non-Darcy Natural Convection in High Porosity Metal Foams, *Int. J. Heat Mass Transf.*, vol. **45**, pp. 3781–3793, 2002.

Petrasch, J., Meier, F., Friess, H., and Steinfeld, A., Tomography based Determination of Permeability, Dupuit–Forchheimer Coefficient, and Interfacial Heat Transfer Coefficient in Reticulate Porous Ceramics, *Int. J. Heat Fluid Flow*, vol. **29**, pp. 315–326, 2008.

Piller, M., Boschetto, A., Schena, G., and Errico, O., Pore-Scale Simulation of Laminar Flow through a Sample of Aluminum Foam, *J. Porous Media*, vol. **16**, pp. 777–793, 2013.

Ranut, P., Nobile, E., and Mancini, L., High Resolution Microtomography-Based CFD Simulation of Flow and Heat Transfer in Aluminum Metal Foams, *Appl. Therm. Eng.*, vol. **69**, pp. 230–240, 2014.

Ranut, P., Nobile, E., and Mancini, L., High Resolution X-Ray Microtomography-Based CFD Simulation for the Characterization of Flow Permeability and Effective Thermal Conductivity of Aluminum Metal Foams, *Exp. Therm. Fluid Sci.*, vol. **67**, pp. 30–36, 2015.

Suleiman, A.S. and Dukhan, N., Forced Convection inside Metal Foam: Simulation over a Long Domain and Analytical Validation, *Int. J. Thermal Sci.*, vol. **86**, pp. 104–114, 2014.

Ucar, E., Mobedi, M., and Pop, I., Effect of an Inserted Porous Layer Located at a Wall of a Parallel Plate Channel on Forced Convection Heat Transfer, *Transp. Porous Media*, vol. **98**, no. 1, pp. 35–57, 2013.

Ucar, E., Mobedi, M., Altintas, G., and Glatt, E., Effect of Voxel Size in Flow Direction on Permeability and Forchheimer Coefficients Determined by using Micro-Tomography Images of a Porous Medium, *Prog. Comput. Fluid Dyn.*, vol. **15**, pp. 327–333, 2015.

Vafai, K., *Handbook of Porous Media*, 3rd ed., Boca Raton, FL: CRC Press, 2015.

Vijay, D., Goetze, P., Wulf, R., and Gross, U., Forced Convection through Open Cell Foams based on Homogenization Approach: Steady State Analysis, *Int. J. Therm. Sci.*, vol. **98**, pp. 381–394, 2015.

Zafari, M., Panjepour, M., Emami, M.D., and Meratian, M., 3D Numerical Investigation of Fluid Flow through Open-Cell Metal Foams using Micro-Tomography, *J. Porous Media*, vol. **17**, pp. 1019–1029, 2014.

Zafari, M., Panjepour, M., Emami, M.D., and Meratian, M., Microtomography-Based Numerical Simulation of Fluid Flow and

Heat Transfer in Open Cell Metal Foams, *Appl. Therm. Eng.*, vol. **80**, pp. 347–354, 2015.

Zhelezny, P.V. and Shapiro, A.A., Experimental Investigation of the Diffusion Coefficients in Porous Media by Application of X-Ray Computer Tomography, *J. Porous Media*, vol. **9**, pp. 275–288, 2006.